RSC Advances

PAPER

View Article Online
View Journal | View Issue

Cite this: *RSC Adv.*, 2025, **15**, 35660

Effect of cobalt doping on the physicochemical and photocatalytic properties of Cu_2BaSnS_4 thin films

Adel Chihi *

Cobalt (Co)-doped Cu_2BaSnS_4 (CBTS) thin films were synthesized *via* the sol–gel dip-coating method to investigate the effect of Co incorporation on their physicochemical properties and photocatalytic activity. X-ray diffraction confirmed that the films crystallize in a trigonal structure, with a slight shift of the favored (104) peak toward higher angles, while X-ray photoelectron spectroscopy verified effective Co incorporation into the CBTS lattice. Surface morphology and roughness, examined by scanning electron microscopy and atomic force microscopy, revealed a reduction in particle size and distinct morphological changes with increasing Co content. UV-vis spectroscopy showed a blueshift in the absorption edge, with the optical band gap widening from 1.78 eV (undoped) to 1.91 eV at 8 at%. The optimized CBTS: Co (6 at%) film achieved 95% degradation efficiency of RhB dye after 120 min and retained high reusability over five cycles. Quenching experiments and electron spin resonance (ESR) analysis identified superoxide radicals ($^{\bullet}O_2^-$) as the dominant reactive species, with the degradation process following pseudo-first-order kinetics. These findings demonstrate that Co doping effectively tunes the physicochemical properties of CBTS thin films, enhancing their photocatalytic efficiency and stability, and highlighting their potential as sustainable, non-toxic, and earth-abundant photocatalysts.

Received 17th July 2025
Accepted 22nd September 2025

DOI: 10.1039/d5ra05156h

rsc.li/rsc-advances

1. Introduction

Chalcogenide semiconductors are emerging as highly promising sustainable materials due to their exceptional chemical and thermal stability, compositional tunability, and adjustable optical and electronic properties. These characteristics make them ideal alternatives to conventional semiconductors, particularly in applications demanding non-toxic, earth-abundant, and cost-effective solutions. Comprising sulfides, selenides, and tellurides, chalcogenides offer remarkable flexibility in tailoring band gaps, carrier concentrations, and crystal structures through compositional modifications and doping strategies. As a result, they have been widely adopted in diverse fields such as photocatalysis, solar cells, and optoelectronics.[1–3] Notably, their efficient visible-light absorption and charge transport capabilities have led to intensive research in photovoltaics, photoelectrochemical cells, and photodetectors. Furthermore, their high dielectric constants, phase-change behavior, and strong infrared absorption make them attractive for applications in phase-change memory, infrared sensors, and optical switching devices.[4] The combination of functional versatility with environmental and economic benefits ranks chalcogenide semiconductors at the forefront of sustainable materials for next-generation technologies. Numerous studies have focused on well-known photocatalysts such as TiO_2, g-C_3N_4, ZnO, and others, all of which are n-type semiconductors with relatively wide band gaps, as widely reported in the literature.[5–7] In contrast, p-type semiconductors photocatalysts have received relatively less attention, despite their promising potential to facilitate improved charge separation. As an emerging candidate in the chalcogenide semiconductor industry, Cu_2BaSnS_4 (CBTS) is an impressive example. Compared to Se or Te-based materials, sulfur-based materials offer advantages thanks to their non-toxic elemental composition and earth-abundant nature, which have been integrated into a wide range of devices for various applications, such as solar cells (dye-sensitized, mesoporous, and planar),[8] and as a photocathode material for photocatalytic water splitting.[9] In addition, CBTS offers potential advantages over its well-known counterpart Cu_2ZnSnS_4 (CZTS), such as reduced cation disorder and improved phase stability owing to the presence of the larger Ba^{2+} ion. Furthermore, CBTS has a suitable band gap (~1.9 eV) and a high optical absorption coefficient (>10^4 cm^{-1}).[10] Nevertheless, the photocatalytic performance of CBTS-based thin films remains limited due to challenges such as suboptimal crystallinity, high resistivity, and significant carrier recombination, often attributed to structural defects and grain boundaries. Various strategies have been employed to enhance the photocatalytic performance of CBTS materials, including tailoring the morphology of the deposited layers, reducing charge carrier recombination through heterojunction formation with other materials, and modifying the catalyst surface to increase the number of active sites.[11] Recently, A. Ali *et al.* showed that CBTS

Photovoltaic Laboratory, Research and Technology Centre of Energy, Borj-Cedria Science and Technology Park, BP 95, 2050 Hammam Lif, Tunisia. E-mail: adel.chihi@crten.rnrt.tn; Fax: +21679325825; Tel: +21654350506

quantum dots are effective for the photocatalytic degradation of organic pollutants and exhibit notable antibacterial properties.[12] Meanwhile, G. Hao *et al.* reported that CBTS nanoparticles showed excellent performance in the removal of methylene blue (MB) with a degradation efficiency of 93% under visible light irradiation within 100 min.[13] Previous studies have explored dopants such as Ge, Sb, Ag, and alkali metals that could enhance the optical, electrical, structural, and morphological properties of CBTS films. So, doping strategies offer a powerful means to tailor the electronic, optical, and structural properties of semiconductors. Employing optimal dopant concentrations and combinations of different dopant elements can significantly enhance electrical and microstructural properties of chalcogenide semiconductor materials, promoting defect passivation. These improvements collectively contribute to superior photocatalytic performance. Transition metal doping, in particular, can influence carrier concentration and enhance trapping of electrons to inhibit electron–hole (e^-/h^+) recombination during irradiation.[14] Previous investigations have demonstrated the effect of Co-doping in many areas, such as the photocatalytic activity of common photocatalysts,[15,16] electromagnetic interference shielding and microwave absorption technologies,[17] photovoltaic applications,[18] and so on. Recently, Co-doped CZTS films have demonstrated notable enhancements in grain size, electrical conductivity, and efficiency of solar cells.[19] To the best of our knowledge, the impact of Co doping on the CBTS semiconductors remains largely unexplored, warranting further investigation.

In this context, the present study investigates the effects of Co doping on CBTS thin films synthesized *via* the sol–gel dip-coating method, with a particular focus on their photocatalytic performance in degrading rhodamine B (RhB) dye under visible light irradiation. Various analytical techniques, including X-ray diffraction (XRD), Raman spectroscopy, X-ray photoelectron spectroscopy (XPS), field emission scanning electron microscopy (FESEM), atomic force microscopy (AFM) and optical absorption and diffuse reflection measurements, were employed to examine the physico-chemical properties of CBTS: Co. Among these, CBTS: Co (6 at%) demonstrated the most notable enhancement in catalytic performance for RhB degradation under visible light irradiation. This improvement is attributed to the synergistic effects of Co doping, which facilitates charge carrier separation, increases conductivity, and introduces beneficial surface states. Besides, electron spin resonance (ESR) spectroscopy and radical quenching experiments confirmed that the high activity of CBTS: Co (6 at%) in RhB degradation is mainly due to the abundant generation of superoxide radicals $^{\bullet}O_2^-$.

2. Experimental details

2.1 Materials and reagents

All reagents used in the synthesis of CBTS films were of analytical grade and obtained from commercial sources. The following chemicals were employed without further purification: copper(II) chloride $CuCl_2$ (97%), barium chloride $BaCl_2$ (99.9%), cobalt chloride hexahydrate $CoCl_2 \cdot 6H_2O$ (≥98.0%), tin(II) chloride dihydrate ($SnCl_2 \cdot 2H_2O$) (≥99.97%), thiourea CH_4N_2S (≥98.0%), hydrogen sulphide H_2S (≥99.5%), lactic acid $C_3H_6O_3$ (100%), ethanolamine C_2H_7NO (≥98%), acetic acid CH_3CO_2H (≥99.7%), ethanol C_2H_6O (≥99.8%), dimethyl sulfoxide C_2H_6OS (DMSO) (99.9%), 2-methoxy ethanol $C_3H_8O_2$ (99.8%), potassium dichromate $K_2Cr_2O_7$ (99.98%), disodium ethylenediaminetetraacetate dihydrate EDTA-Na_2 (>99%), isopropanol IPA (>99%), *p*-benzoquinone *p*-BQ (>99.5%), 5-*tert*-butoxycarbonyl-5-methyl-1-pyrroline-*N*-oxide BMPO (≥99.0%), 5,5-dimethyl-1-pyrroline *N*-oxide DMPO (≥98%), and 2,2,6,6-tetramethylpiperidine-1-oxyl TEMPO (≥98%). All reagents mentioned above were purchased from Sigma-Aldrich. Deionized (DI) water with a resistivity of 18 MΩ cm was utilized in preparing solutions and rinsing the samples. Indium-doped tin oxide (ITO) conductive glass slides, cut to a size of 2 × 2 cm (thickness of 2.0 mm, resistivity of 5 Ω sq^{-1}, and transmittance exceeding 80%), were used as substrates for the deposition of CBTS: Co thin films.

2.2 Materials synthesis

The CBTS precursor solution was synthesized by dissolving 1 mM of $CuCl_2$, 0.5 mM of $BaCl_2$, 0.5 mM of tin(II) $SnCl_2 \cdot 2H_2O$, and 2 mM of CH_4N_2S in 100 mL of DMSO solvent. Then, the solution was stirred vigorously for 30 min and aged for 24 hours under ambient conditions. Meanwhile, a few drops of $C_3H_6O_3$ were added to the DMSO solvent under agitation at 323 K to enable the dissolution of barium. To incorporate cobalt into CBTS films, $CoCl_2 \cdot 6H_2O$ was used as the cobalt precursor at four different atomic percentages. The undoped and Co-doped CBTS precursor solutions (2 at%, 4 at%, 6 at%, and 8 at%) were prepared in a solvent mixture of $C_3H_8O_2$ and DMSO, and then uniformly magnetically stirred at 333 K for 1 hour to ensure complete dissolution and homogeneity. Prior to the experiments, ITO glass substrates were thoroughly cleaned with deionized (DI) water, followed by ultrasonic cleaning for 20 min. The substrates were then dried in an oven at 373 K for 60 min. Dip-coating of the prepared solution was carried out using a dip coater mounted on an anti-vibration platform. Each substrate was sequentially immersed in five separate solutions for 5 min each, with a withdrawal speed of 50 mm min^{-1} and a dwell time of 20 s. After coating, the substrates were left to dry overnight in a storage box. All experimental procedures were conducted within a ventilated enclosure to ensure safety and prevent contamination. Annealing was performed at 700 K for 10 min using rapid thermal processing (RTP) equipped with infrared (IR) heating lamps, under a mixed atmosphere of nitrogen and 30% hydrogen sulfide (H_2S) to minimize sulfur loss. The samples were subsequently cooled to room temperature (~300 K) before characterization. Finally, the CBTS film thickness was measured using a Bruker Dektak XT contact profilometer, assuming uniform and dense films, and was found to be approximately 1.2 μm.

2.3 Apparatus and measurements

X-ray diffraction (XRD) patterns were recorded at room temperature in Bragg–Brentano geometry using an X-ray diffractometer instrument (model Philips-Xpert) equipped

with Cu-K_α radiation ($\lambda = 1.54$ Å). Data were collected over a 2θ range of 10° to 70°, with a step size of 0.05°. Phase identification was carried out using HighScore software from PANalytical.[20] Confocal Raman spectroscopy was performed using a 632.8 nm He–Ne laser source (HORIBA Scientific), and the Raman shift was calibrated by the single crystal Si at 520.4 cm^{-1}. The surface morphology of the deposited films was examined using a field emission scanning electron microscope (FESEM, JEOL JSM-5400). Atomic force microscopy (AFM) images were acquired in tapping mode using a Bruker dimension icon XR AFM. Quantitative surface roughness parameters were evaluated with the Gwyddion software package.[21] The binding energies of all constituent elements were determined using an ESCALAB 250 X-ray photoelectron spectrometer (Thermo Fisher Scientific). To study the optical characteristics, the optical absorption and diffuse reflection measurements of the films were recorded using a PerkinElmer lambda 950 spectrophotometer equipped with an integrating sphere, in the wavelength range of 400–1200 nm. Electron spin resonance (ESR) measurements were carried out using a Bruker ELEXSYS E580 FT/CW spectrometer operating at a microwave frequency of approximately 9.7 GHz. Magnetic field modulation was applied to enhance signal detection, and all measurements were conducted at room temperature.

2.4 Photocatalytic studies

The RhB dye was dissolved in a 100 mL beaker containing DI water to prepare a concentration of 5 mg L^{-1}. All the CBTS: Co films with a surface area of 1 × 1 cm^2 were immersed in RhB aqueous solutions in separate 20 mL glass beakers. Subsequently, all solutions were magnetically stirred in the dark for 20 min to establish adsorption–desorption equilibrium between the RhB dye molecules and the photocatalyst surfaces. The RhB concentration at equilibrium was regarded as the initial concentration, C_0, for subsequent photocatalytic experiments. Photodegradation experiments were carried out under visible light illumination provided by a 300 W xenon lamp equipped with a cut-off filter ($\lambda \geq 420$ nm). The photocatalytic reaction was allowed to proceed for 120 min under continuous stirring. The beaker containing the reaction mixture was positioned about 10 cm from the xenon lamp. Radical trapping experiments were performed using specific scavengers to identify the active species involved in the photocatalytic process. (IPA, 2 mL) hydroxyl radicals ($^{\bullet}OH$), (*p*-BQ, 0.05 g) for superoxide radicals ($^{\bullet}O_2^-$), ($K_2Cr_2O_7$, 0.05 g) for photoinduced electrons (e^-), and (EDTA-Na_2, 0.05 g) for photoinduced holes (h^+). All the above reactions were carried out at room temperature.

3. Results and discussions

3.1 Structural analysis

Fig. 1a presents the XRD patterns of all CBTS: Co films deposited on ITO conductive glass substrates at varying Co doping levels from 0 at% to 8 at%. All samples, including the undoped CBTS film, exhibit well-defined and sharp diffraction peaks that are consistent with the trigonal crystal structure of the CBTS phase (JCPDS card no. 030-0124), corresponding to the $P3_1$ space group symmetry with the lattice parameters $a = 6.3670$ Å, $b = 6.3670$ Å, $c = 15.8830$ Å and a unit cell volume $V = 566.03$ $Å^3$.[22] It can also be observed that an additional minor peak marked with a red dot is attributed to the underlying ITO glass substrate (JCPDS card no. 06-0416). The undoped CBTS film exhibits a strong preferential orientation along the (104) plane at $2\theta \cong 27.7°$. Nevertheless, as the Co doping level increases, this dominant peak shifts towards higher diffraction angles, as shown in Fig. 1b. This shift is likely attributed to Co substitution in the lattice, given that the ionic radius of Co^{2+} (0.745 Å)[23] is considerably smaller than that of Ba^{2+} (1.350 Å).[24] The slight shift of the main diffraction peak (104) to a higher angle substantiates the existence of compressive strain within the lattice due to substitutional Co doping. It is noteworthy that in the sample doped with 8 at% Co, additional diffraction peaks corresponding to cobalt sulfide (Co_3S_4) (JCPDS card no. 75-1561) were observed at 2θ values of 26.81°, 31.54°, 38.27°, 50.41°, and 55.24°, which align with the (220), (311), (400), (511), and (440) planes, respectively.[25] Despite a sulfur-rich and reducing atmosphere, the formation of Co_3S_4 may be attributed to the combined effects of short annealing duration, moderate

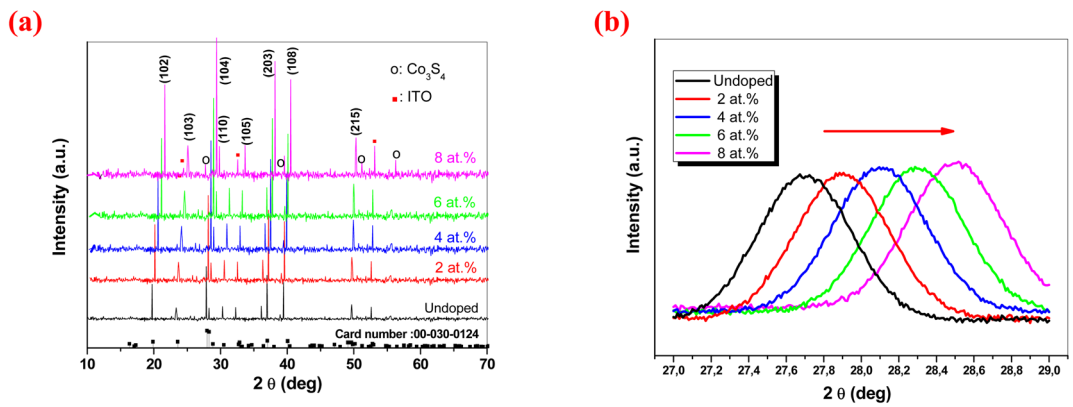

Fig. 1 (a) XRD patterns of undoped and Co-doped CBTS thin films deposited by the dip-coating technique at various Co concentrations. (b) Magnified view of the (104) diffraction peak highlighting the systematic peak shift induced by Co incorporation.

sulfur activity, and partial oxidation during the cooling phase. These peaks indicate the onset of secondary phase formation at higher doping levels. The emergence of Co_3S_4 suggests the segregation of Co, thereby reducing the effective incorporation of Co into the CBTS crystal lattice. Such phase segregation can lead to increased defect states and charge carrier recombination centres, ultimately degrading the photocatalytic properties of the CBTS material. Additionally, the appearance of Co_3S_4 may influence grain boundary behavior and hinder uniform crystal growth, which could negatively impact charge transport across the CBTS absorber layer. Therefore, careful control of Co doping concentration is critical to ensure phase purity and to optimize the electrical and photocatalytic performance of CBTS films.

According to the favored diffraction peak of the (104) plane, the average crystallite size was assessed using the Debye–Scherrer equation:[26]

$$D = \frac{K\lambda}{\beta_{hkl}\cos\theta} \quad (1)$$

where K is a dimensionless shape factor, with a typical value of 0.94 for spherical crystallites; λ is the wavelength of the X-ray radiation (1.5418 Å), while β_{hkl} (rad) and θ are full width at half maximum (FWHM) and Bragg's angle, respectively. The FWHM of the XRD peaks for all CBTS: Co thin film samples gradually increases with increasing Co doping level. This broadening of the diffraction peaks signifies a reduction in crystallite size, consistent with the Scherrer equation, and also indicates an increase in microstrain and lattice imperfections. Fig. 2 displays the variation in the crystallite size of CBTS: Co films *versus* the Co doping level. The crystallite size of CBTS: Co films decreases progressively with increasing Co doping level up to 6 at%. This reduction in crystallite size is primarily attributed to the ionic radius mismatch between the substituting Co ions and the host Ba ions in the CBTS lattice, as mentioned earlier. These structural disruptions hinder the coalescence and the growth of crystalline grains, resulting in a decrease in average crystallite size and an increase in defect density. Nevertheless, at higher Co doping levels (*i.e.*, 8 at%), the crystallite size remains approximately constant. This behaviour is likely due to the onset of secondary phase formation, specifically the appearance of Co_3S_4 clusters, as indicated by an additional diffraction peak in the XRD patterns. The formation of Co_3S_4 suggests that the CBTS lattice becomes saturated with Co beyond 6 at%, leading to phase separation. In this scenario, excess Co atoms no longer integrate into the host lattice but instead segregate to form a distinct Co-rich phase, which can locally relax the strain and enable grain coarsening. On the other hand, the lattice microstrain (ε) and dislocation density (δ) were evaluated based on XRD data, by applying the following equations:[27]

$$\varepsilon = \frac{\beta\cos\theta}{4} \quad (2)$$

$$\delta = \frac{1}{D^2} \quad (3)$$

As shown in Fig. 2, both microstrain and dislocation density slightly increase with Co doping up to 6 at%, reaching maximum values of approximately 8.86×10^{-5} and 1.80×10^{-4} lines per nm^2, respectively. This increase suggests enhanced lattice distortion and defect density, which can promote charge separation and provide more active sites, potentially improving the CBTS: Co photocatalytic performance.

3.2 Raman analysis

Raman spectroscopy is a prevailing tool for unequivocally identifying the vibrational modes of CBTS films as a function of Co doping level. As depicted in Fig. 3, all synthesized samples exhibit four distinct Raman-active modes under 632.81 nm laser excitation, with a dominant peak at 340 cm^{-1}, characteristic of the trigonal CBTS phase.[28] The vibrational modes observed at 192, 249, 340, and 364 cm^{-1} correspond to totally symmetric (A-symmetry) vibrations (see Table S1), mainly involving displacements of sulfur atoms.[29] Nevertheless, as the Co doping level increases from 0 to 8 at%, the full width at half maximum (FWHM) of all peaks gradually broadens from ~1 cm^{-1} to ~2 cm^{-1}, indicating reduced crystallinity and an elevated defect density. A weak peak emerges near 381 cm^{-1} in

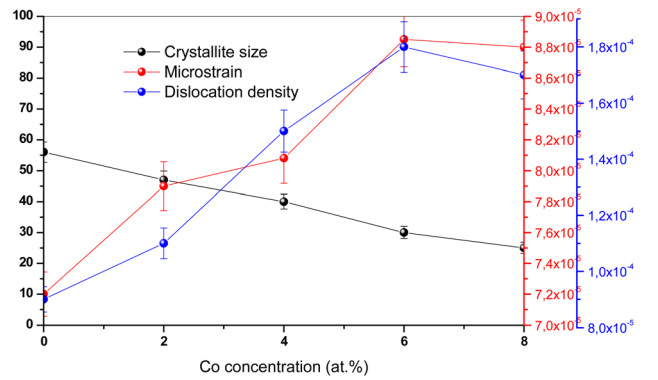

Fig. 2 Variation of crystallite size, microstrain and dislocation density as a function of Co doping levels in CBTS thin films.

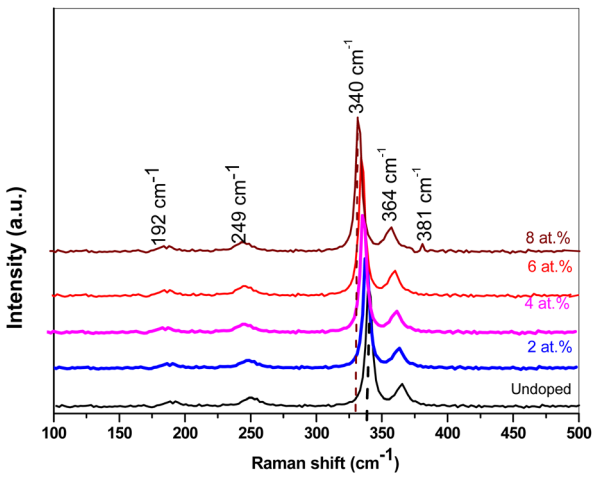

Fig. 3 Raman spectra of CBTS thin films with varying Co doping levels, showing the evolution of characteristic vibrational modes.

the sample doped with 8 at%, which is probably due to the formation of a secondary Co_3S_4 phase.[30,31] The found peak at 381 cm^{-1} corresponds to the A_g vibrational mode, originating from the symmetric bending vibrations of S–Co–S units.[32] This result is in good agreement with the above XRD analysis. Moreover, a slight redshift of prominent modes suggests lattice expansion and bond weakening. Overall, both XRD and Raman analyses confirm that maintaining an optimal doping level is crucial for preserving the crystallinity and phase purity of CBTS films. This doping level greatly influences the transport of photo-generated electrons and holes to the CBTS film surface, thereby affecting the photocatalytic performance.

3.3 XPS analysis

X-ray photoelectron spectroscopy (XPS) is a non-destructive technique that provides detailed information about the elemental composition, chemical states, and electronic structure of a material.[33] By analyzing the binding energy of the core electrons, XPS can reveal the oxidation states of Cu, Ba, Co, Sn, and S elements in both undoped and Co-doped CBTS films. This is essential for understanding the material's electronic properties and its potential applications in photocatalytic activity. Fig. 4(a) presents the XPS survey spectra of both undoped and Co-doped CBTS (8 at%) films, recorded over the binding energy range of 0 to 1200 eV. As can be seen by comparing the XPS survey spectra of undoped and Co-doped CBTS (8 at%), the presence of the Co element confirms the successful incorporation of Co into the CBTS lattice. The other Co-doped CBTS films exhibit XPS profiles similar to that of the undoped sample, with the notable emergence of additional peaks corresponding to Co binding energies (not shown). This XPS behavior could be attributed to the fact that Co doping does not significantly modify the chemical state or bonding environment of the core CBTS elements within the detection limits of XPS. However, a slight contamination from oxygen and carbon was detected at 532.2 eV and 284.6 eV, respectively. This

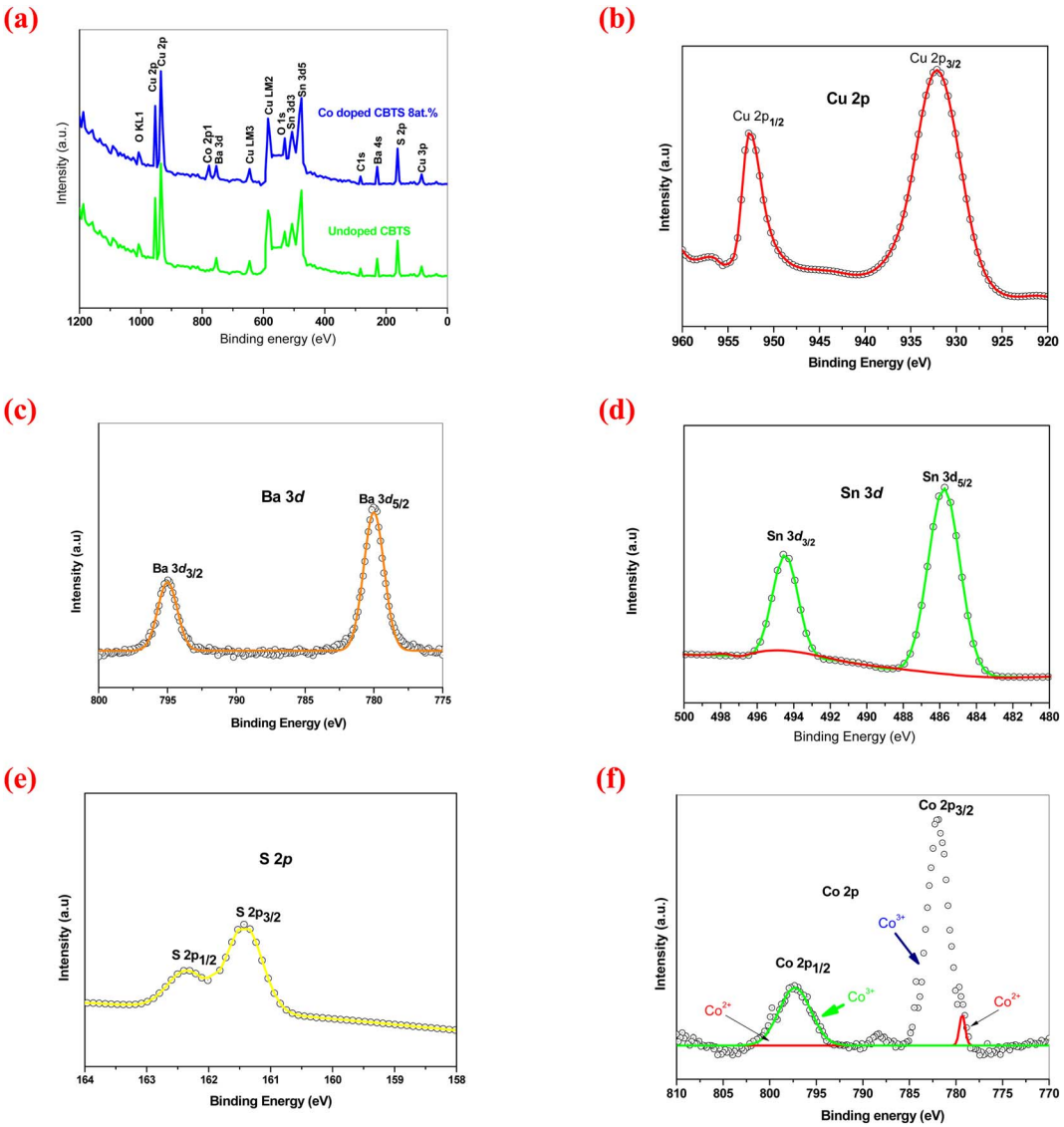

Fig. 4 XPS spectra of (a) undoped and Co-doped CBTS (8 at%), (b) Cu 2p, (c) Ba 3d, (d) Sn 3d, (e) S 2p, (f) Co 2p.

can be attributed to surface impurities and the formation of reactive oxide species upon exposure of the chalcogenide films to the atmospheric environment.[27] To further examine the chemical states of Cu, Ba, Sn, S, and Co in CBTS films, XPS analysis was conducted on all samples. All the following XPS core-level spectra were fitted with a high *R*-squared value of 0.998, demonstrating the high accuracy of the fit and the reliable identification of the chemical states of each element resulting from doping. Fig. 4(b–f) exhibits the core level spectra of Cu 2p, Ba 3d, Sn 3d, S 2p, and Co 2p obtained from the XPS analysis of the undoped CBTS sample. It can be observed from Fig. 4b that the Cu 2p spectrum displays fitted peaks at 932.1 eV ($2p_{3/2}$) and 951.9 eV ($2p_{1/2}$), matching a spin–orbit splitting of 19.8 eV, which is assigned to Cu^{+} species.[34] Notably, no satellite peaks were detected at higher binding energies, confirming the absence of Cu^{2+} and indicating that Cu^{2+} ions were reduced to Cu^{+} during the synthesis process. The Ba 3d spectrum (Fig. 4c) exhibits fitted peaks at 779.2 ($3d_{3/2}$) and 794.5 eV ($3d_{5/2}$), with

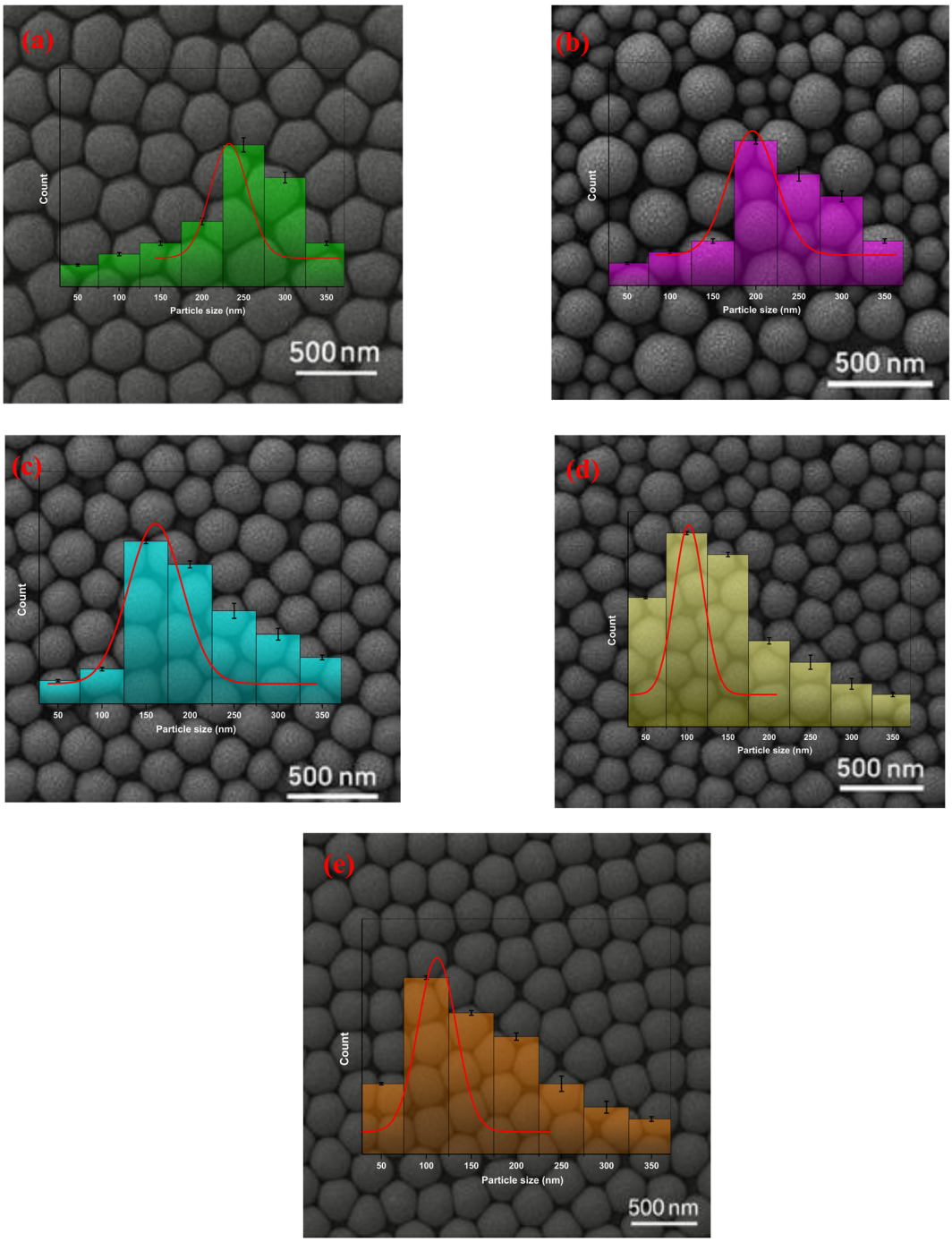

Fig. 5 Top-view SEM images of (a) undoped CBTS, (b) 2 at% Co-doped, (c) 4 at% Co-doped, (d) 6 at% Co-doped, and (e) 8 at% Co-doped CBTS thin films.

a splitting energy of 15.3 eV, consistent with the Ba^{2+} oxidation state.[35] As shown in Fig. 4d, the fitted peaks at binding energies of 486.2 eV and 494.8 eV correspond to $3d_{5/2}$ and $3d_{3/2}$, respectively, with a spin–orbit splitting of 8.6 eV, in agreement with the Sn^{4+} oxidation state.[36] Fig. 4e shows the S 2p spectrum, which is deconvoluted into two fitted peaks at 161.35 eV ($2p_{3/2}$) and 162.55 eV ($2p_{5/2}$), with a spin–orbit splitting of 1.20 eV, confirming that sulfur is present in the S^{2-} oxidation state.[27] The abovementioned outcomes display that the surface of the CBTS films contains Cu^{+}, Ba^{2+}, Sn^{4+}, and S^{2-} ions. However, for the Co-doped CBTS films, the XPS spectra exhibit additional peaks corresponding to the Co element. Fig. 4f shows Co $2p_{3/2}$ and Co $2p_{1/2}$ fitted peaks at 781.2 eV and 796.8 eV, respectively, with a spin–orbit splitting of 15.6 eV, along with two shakeup satellites at approximately 786.6 eV and 804.2 eV.[37] To reveal the chemical state of Co and its incorporation into the CBTS lattice, the Co 2p spectra were deconvoluted to resolve overlapping Co $2p_{3/2}$ and Co $2p_{1/2}$ core levels and distinguish between different Co oxidation states. The Co $2p_{3/2}$ peak was deconvoluted into two components at 781.0 eV (Co^{2+} $2p_{3/2}$) and 782.6 eV (Co^{3+} $2p_{3/2}$). Similarly, the Co $2p_{1/2}$ peak was deconvoluted into two peaks at 796.6 eV (Co^{2+} $2p_{1/2}$) and 798.2 eV (Co^{3+} $2p_{1/2}$). These results confirm the mixed oxidation state in the Co-doped CBTS films (8 at%), consistent with the previous studies.[38,39] As we know, Co

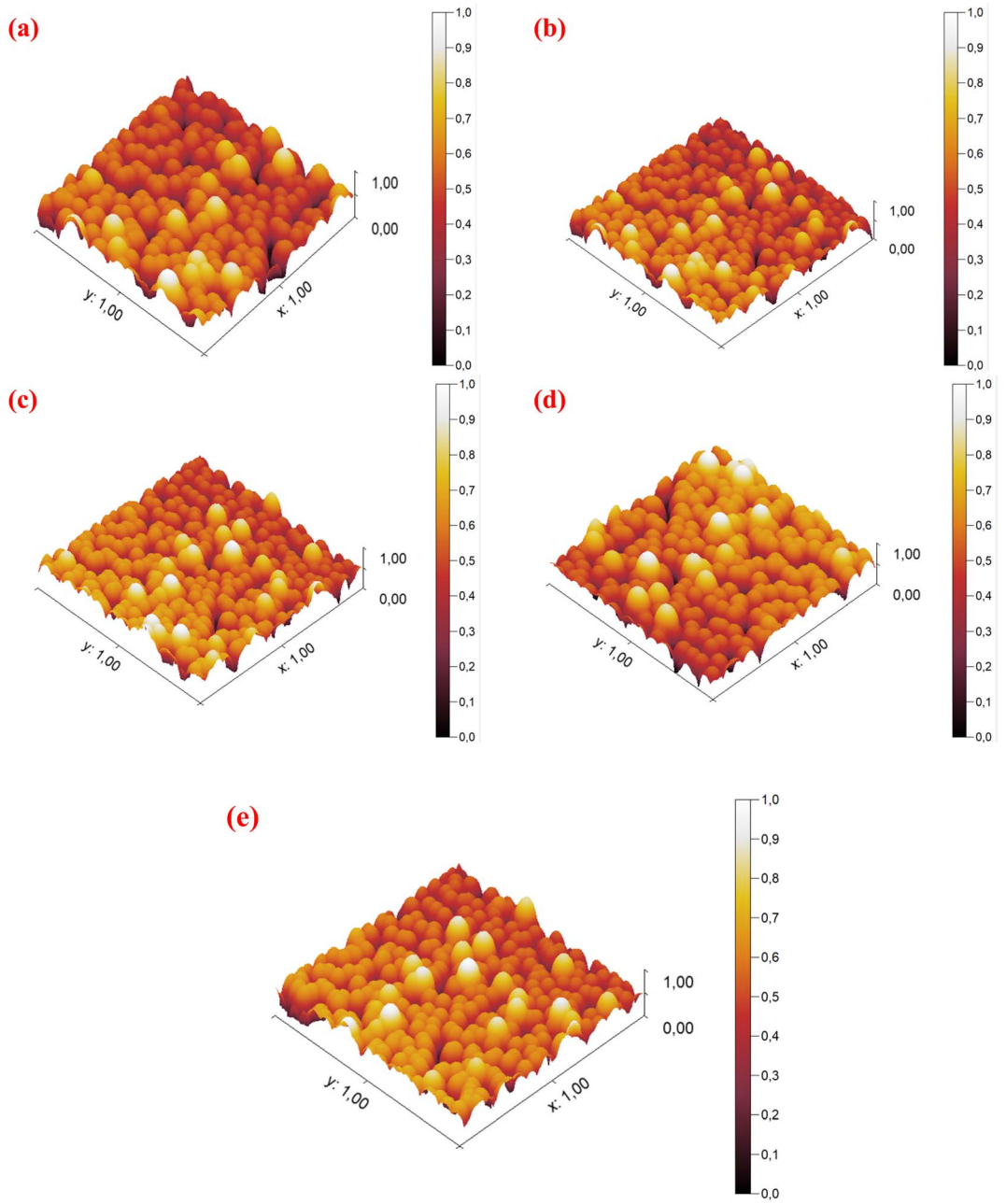

Fig. 6 3D AFM images of (a) undoped CBTS, (b) 2 at% Co-doped, (c) 4 at% Co-doped, (d) 6 at% Co-doped, and (e) 8 at% Co-doped CBTS thin films.

exists in two oxidation states, Co^{2+} and Co^{3+}, each exhibiting distinct ionic radii and chemical behaviors. The relative dominance of Co oxidation states significantly affects its incorporation into the CBTS lattice; however, contrary to expectations promoting Co^{3+} at lower doping levels, our results reveal that Co^{2+} is the predominant oxidation state in the Co-doped CBTS films. The actual chemical environment, synthesis conditions (*e.g.*, sol–gel dip-coating, annealing atmosphere), or thermodynamic stability of Co^{2+} favours the two-oxidation state in our films. This unexpected distribution of oxidation states significantly influences the structural development of the material, affecting lattice distortion, guiding the nucleation of secondary phases such as Co_3S_4, and consequently impacting both the crystallite size and film morphology. Overall, the binding energy values for Cu, Ba, Co, Sn, and S obtained in the present work are in good agreement with those reported in the literature,[27] further confirming the successful incorporation of Co into the CBTS lattice *via* the dip-coating method.

3.4 SEM and AFM characterization

To scrutinise the effect of Co doping on the microstructure, grain size, and roughness of CBTS films, SEM and AFM measurements were carried out on CBTS films. As shown in Fig. 5, top-view SEM images of all CBTS films displayed mixed and densely packed spherical particles grown on the ITO substrate. The average particle size for the undoped sample is approximately 250 nm. However, as the Co doping level increases from 0 to 8 at%, the particle size gradually decreases, reaching values as small as 100 nm. The inset of Fig. 5a–e displays the particle size statistics for all samples, with average particle sizes determined using Gwyddion software.[21] The results indicate that the sample with a Co doping level of 6 at% exhibits the smallest particle size. The reduction in particle size of CBTS films is of great advantage for photocatalytic applications, as it increases the surface area and enhances charge carrier separation by shortening diffusion paths, thereby promoting more efficient redox reactions at the CBTS catalyst surface. By comparing the SEM and XRD measurements, it was found that the average particle sizes of the CBTS samples, as determined from SEM images, are approximately five times larger than the crystallite sizes estimated from the Scherrer equation. This indicates that the particles in the SEM images were composed of several nanocrystallites. Fig. 6 presents the 3D AFM images of both undoped and Co-doped CBTS films, recorded at the scale of $1 \times 1\ \mu m^2$. As can be shown, the AFM images reveal significant morphological changes with increasing Co doping levels, indicating a clear dependence of surface topography on chemical composition. The undoped sample displays random grains with quite uniform spherical shapes spread across the surface, which aligns well with the SEM findings analysis. In contrast, increasing Co doping levels led to a progressive deterioration of the surface morphology, as demonstrated by the formation of less compact and more irregularly shaped grains, as shown in Fig. 6b–e. This morphological evolution suggests that higher Co doping levels result in decreased compaction and increased surface roughness. Fig. 7 illustrates that both the root mean square roughness (R_q) and the arithmetic mean roughness (R_a) gradually increase with rising Co doping levels. The observed increase in R_q and R_a with Co doping indicates that Co incorporation alters the surface morphology of CBTS films, resulting in progressively rougher surfaces. This is likely attributed to changes in grain growth dynamics, nucleation behavior, and lattice strain induced by the substitution of Co into the CBTS lattice. Overall, AFM images revealed that the surface roughness increases with Co doping up to 6 at%, resulting in an enhanced specific surface area.

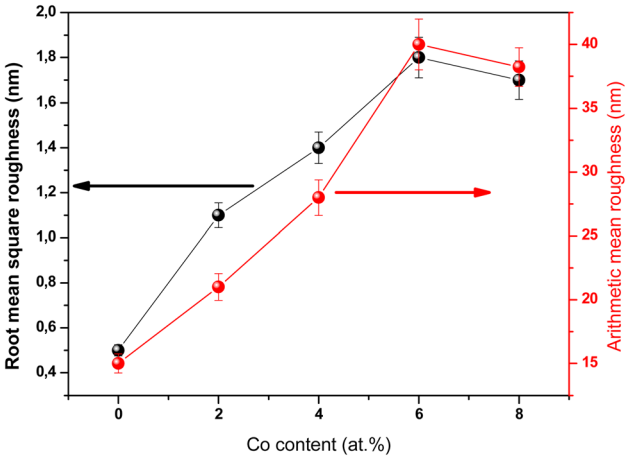

Fig. 7 Evolution of root mean square roughness and arithmetic mean roughness *versus* Co content in CBTS films.

3.5 Optical analysis

The linear optical properties of undoped and Co-doped CBTS films grown on an ITO substrate have been derived from transmittance $T(\lambda)$ and reflectance $R(\lambda)$ measurements in the wavelength range of 400–1200 nm. Fig. 8a and (b) illustrate the $T(\lambda)$ and $R(\lambda)$ plots of all synthesized samples at various Co doping levels. The $T(\lambda)$ spectra of the CBTS films decrease progressively from 80% to 60%, while the corresponding $R(\lambda)$ spectra increase from 2% to 20%, as the Co doping level rises from 0 to 8 at%. It is worth noting that the presence of interference oscillations in both spectra confirms the uniformity and homogeneity of the synthesized CBTS films *via* the dip coating process. On the other hand, the absorption coefficient $\alpha(\lambda)$ values of the undoped and Co-doped CBTS films were estimated using the following formula:[40]

$$\alpha(\lambda) = \frac{1}{d}\ln\left(\frac{(1-R)^2 + \left((1-R)^4 + 4R^2T^2\right)^{1/2}}{2T}\right) \quad (4)$$

In this relation, d refers to the film thickness. Fig. 9a illustrates the graph of $\alpha(\lambda)$ as a function of wavelength for undoped and Co-doped CBTS films. The $\alpha(\lambda)$ values decrease with increasing Co doping levels. Moreover, the spectra exhibit a gradual blue-shift in the absorption edge, indicating modifications in band structure induced by Co incorporation. On the other hand, the

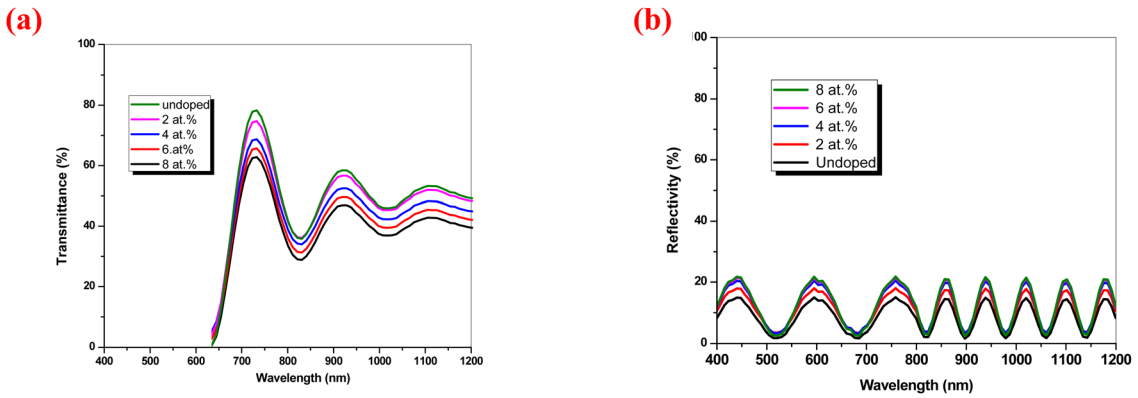

Fig. 8 (a) The transmission and (b) reflectance spectra of Co-doped CBTS thin films, recorded at different Co doping levels.

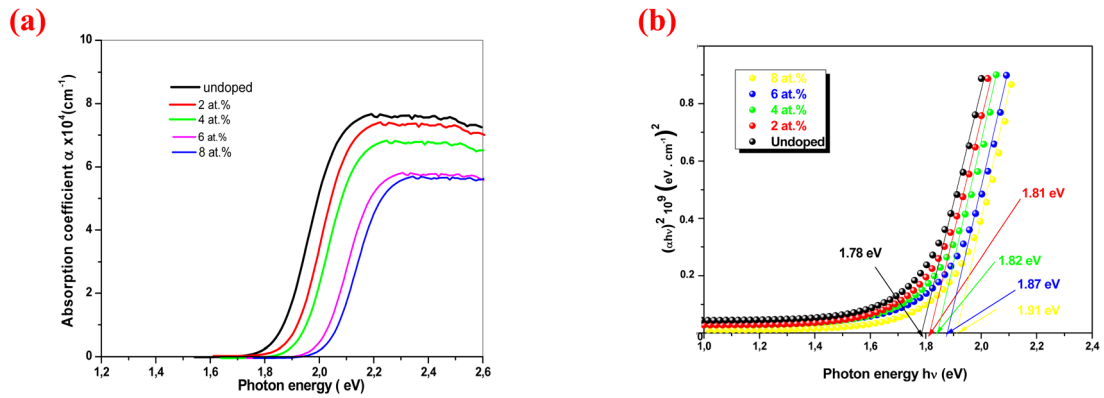

Fig. 9 (a)The absorption spectra for thin layers of cobalt-doped CBTS at different doping concentrations. (b) Effect of Co-doping on the optical band gap of CBTS films derived from Tauc analysis.

optical band gap of all samples was evaluated in the strong absorption region ($\alpha > 10^4$ cm^{-1}) *via* Tauc's equation:[41]

$$\alpha h\nu = B(h\nu - E_g)^p$$

where E_g, B, and p stand for the optical bandgap, the Tauc parameter, and the exponent factor, respectively. The Tauc parameter B is associated with the transition probability, while the exponent p determines the nature of the electronic transition. The value of p varies depending on the type of transition: $p = 1/2$ for direct allowed, $p = 2$ for indirect allowed, $p = 3/2$ for direct forbidden, and $p = 3$ for indirect forbidden transitions. This study reveals that optimal fitting occurs at $p = 1/2$, suggesting allowed direct optical transitions. Fig. 9b shows the plot of $(\alpha h\nu)^2$ *versus* $h\nu$ for the examined Co-doped CBTS films. The E_g value of these samples can be determined from the x-axis intercept of this graph. We observe a gradual increase in E_g from 1.78 eV to 1.91 eV with increasing doping level. The observed blueshift in band gap energy can be attributed to quantum confinement effects arising from reduced crystallite size, as well as structural modifications and lattice strain induced by Co incorporation into the CBTS lattice. Similar effects have been reported in other previous studies.[42] Meanwhile, the Urbach energy (E_u) of the examined Co-doped CBTS films was determined by the relationship:[43]

$$\alpha(\nu) = \alpha_0 \exp\left(\frac{h\nu}{E_u}\right) \quad (5)$$

where α is the absorption coefficient, hν is the photon energy, E_g is the optical band gap, E_u is the Urbach energy, and α_0 is a constant.

Taking the logarithm of the above equation yields the following expression:

$$\ln(\alpha) = \ln(\alpha_0) + \frac{h\nu}{E_u} \quad (6)$$

The E_u was estimated from the inverse slope of the linear region in the $\ln(\alpha)$ *versus* $h\nu$ plot, as shown in Fig. 10a. The variation of E_u and E_g values against Co doping is demonstrated in Fig. 10b. The values reveal that E_u decreases from 0.75 eV to 0.31 eV as the Co content increases from 0 to 8 at%. Additionally, these plots display an inverse relationship between E_u and E_g, which is consistent with earlier findings for many other materials.[44] The minor reduction in E_u reflects a more ordered atomic arrangement within the CBTS lattice, indicating enhanced crystallinity following Co ion doping. This leads to

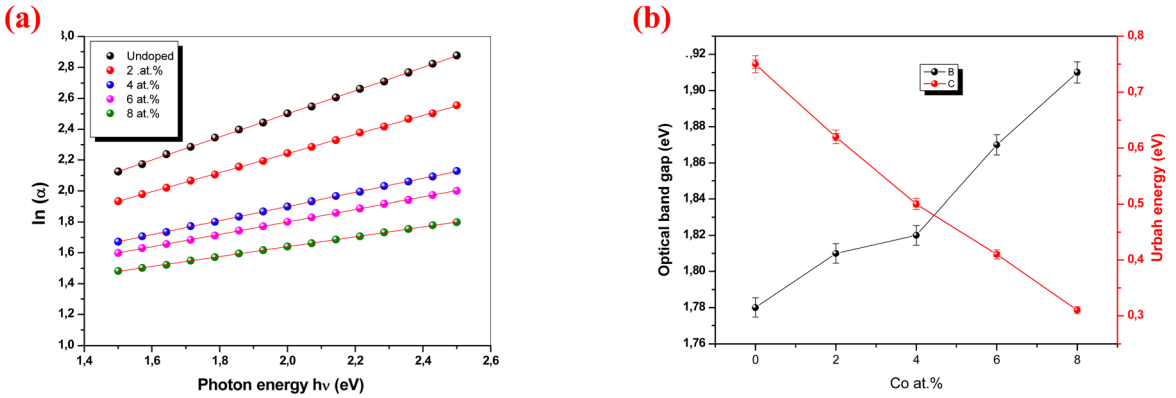

Fig. 10 (a) Variation of ln (α) *versus* photon energy, (b) variation of optical band gap and Urbach energy *versus* Co doping level.

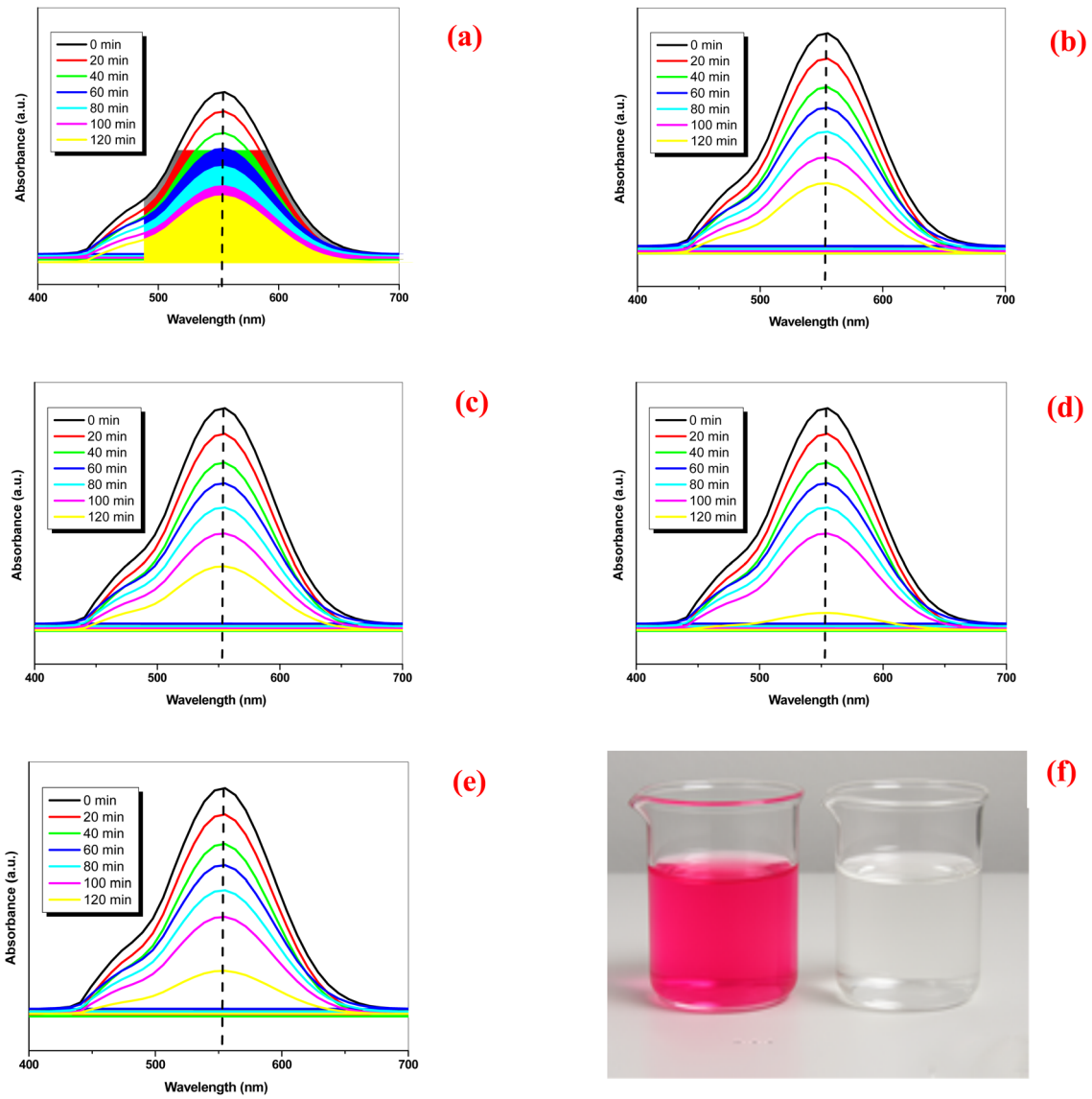

Fig. 11 (a–e) The temporal evolution of the absorbance spectra of the RhB dye solution in the presence of both undoped and CBTS: Co films. (f) The colour of the RhB solution altered from a bright opera rose to nearly colourless in the presence of CBTS film.

decreased localised states and reduced energetic disorder at the band edges, characteristic of structurally ordered semiconductors.[45]

3.6 Photocatalytic RhB removal activity assessment

RhB is classified as a potential carcinogen by the International Agency for Research on Cancer (IARC) and poses serious environmental and health risks. Given its persistence in wastewater, RhB was selected as a model pollutant in this study. Semiconductor photocatalysis offers an energy-efficient, cost-effective approach for its degradation. The temporal evolution of the absorbance spectra of the RhB dye solution was monitored under visible light irradiation at 20-min intervals in the presence of both undoped and CBTS: Co films, as illustrated in Fig. 11a–e. The photocatalytic degradation of RhB is minimal with undoped CBTS films. However, a significant drop in the intensity of the main absorption peak at 554 nm was observed over time following Co doping, indicating the gradual decomposition of the RhB dye. Notably, around 91% of the dye was degraded within 120 min of illumination in the presence of the CBTS: Co film with 6 at%, demonstrating excellent photocatalytic activity. In contrast, only 60% degradation was achieved with the undoped CBTS film under the same conditions. Moreover, the colour of the solution visibly altered from a bright opera rose to nearly colourless, as shown in Fig. 11f, further confirming the degradation process. Importantly, no significant shift in the λ_{max} of RhB dye was detected during the photoreaction in the absorbance spectrum, indicating that the degradation pathway does not involve molecular structural transformation or *N*-deethylation but proceeds mainly through photocatalytic mineralisation mechanisms. The photocatalytic degradation rate of RhB dye was evaluated using the following equation:[46]

$$D_e(\%) = \left(1 - \frac{C_t}{C_0}\right) \times 100 \quad (7)$$

where D_e, C_0 and C_t (mg L^{-1}) represent the degraded efficiency (%), the initial concentration of RhB before the reaction and the concentration remaining at time t, respectively.

As depicted in Fig. 12a, all samples exhibited a slight reduction in RhB concentration under dark conditions, suggesting minimal dye adsorption onto the CBTS: Co film surfaces. This negligible degradation confirms that physical adsorption alone does not significantly contribute to the removal of RhB dye. In contrast, upon exposure to visible light (λ > 420 nm), a pronounced increase in the photocatalytic degradation rate of RhB was observed across all doping samples, as shown in Fig. 12(b). This enhancement highlights the crucial role of photoexcited charge carriers generated within the CBTS: Co films, which drive the degradation of RhB under light illumination. The results demonstrate that the photocatalytic degradation process is light-dependent, with Co doping playing a significant role in optimizing visible-light absorption and charge carrier dynamics. The rise in photocatalytic degradation with increasing Co doping levels is attributed to the generation of (e^-/h^+) pairs under visible light irradiation. On the other hand, the CBTS: Co film with 6 at% doping exhibited the highest photocatalytic activity, reaching 95% RhB degradation after 120 min, which is 61% higher than that of the undoped one, due to its superior surface roughness, smallest crystallite size, and relevant band gap. Nevertheless, excessive doping may lead to the formation of secondary phases such as Co_3S_4, which could adversely affect the photocatalytic rate. Indeed, the existence of the Co_3S_4 phase can promote charge carrier trapping and recombination centres, reducing carrier lifetime and mobility. What is more, it can serve as an insulating barrier that enhances resistivity and hinders efficient carrier movement. Compared with widely studied photocatalytic systems such as composites (*e.g.*, WS_2@PPy nanocomposites[47]), doped photocatalysts (*e.g.*, Cu-doped ZnO,[48] Eu/Fe co-doped Bi_2WO_6 (ref. 49)), heterojunctions (*e.g.*, Sb_2MoO_6/g-C_3N_4 (ref. 50)), and perovskite-based photocatalysts (*e.g.*, $(Na_{0.5}Bi_{0.5})$ ZrO_3 (ref. 51)), the Co-doped CMTS thin films developed in this study offer distinct advantages. These include high degradation efficiency under visible light, shorter reaction times, and a simple, low-cost synthesis route that does not require co-catalysts or sacrificial agents. Notably, under visible-light irradiation, CMTS: Co significantly outperforms the perovskite-type photocatalyst $(Na_{0.5}Bi_{0.5})$ ZrO_3, which achieves

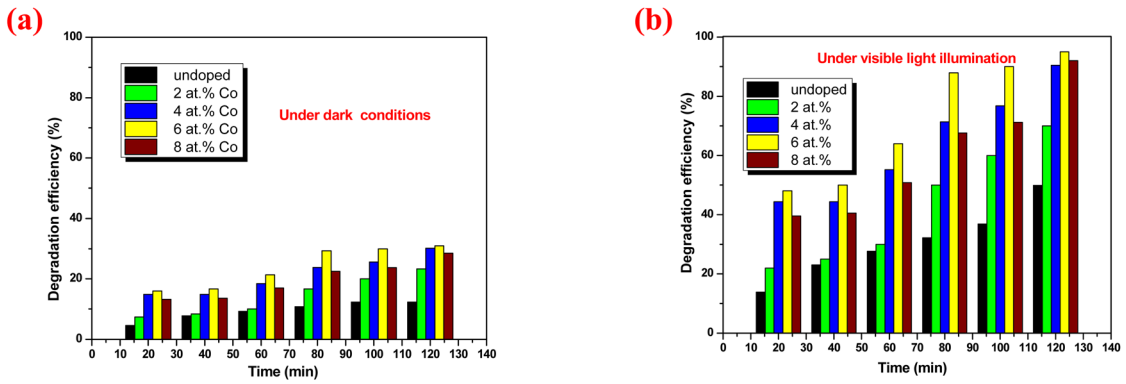

Fig. 12 Photocatalytic degradation efficiency of RhB dye using Co-doped CBTS films (a) under dark conditions and (b) under visible light irradiation.

Table 1 Comparative summary of cobalt-doped CBTS photocatalyst from the present work with other reported studies, highlighting the synthesis method, reaction time, and photocatalytic performance

Study	Synthesis method	Photocatalyst	Target pollutant	Light source	Degradation efficiency (%)	Time (min)
47	Chemical oxidative polymerization	WS_2@PPy nanocomposite	RhB	Visible light	99	90
48	Precipitation	Cu-doped ZnO	RhB	UV irradiation	100	120
49	Hydrothermal method	Eu/Fe Co-doped Bi_2WO_6	RhB	Visible light	99	6
50	Physical mixing	Sb_2MoO_6/g-C_3N_4 heterojunction	RhB	UV-visible light	94	40
51	Solid-state	$(Na_{0.5}Bi_{0.5})$ ZrO_3	RhB	Visible light	68	180
Present study	Sol–gel (dip coating)	CBTS: Co	RhB	Visible light	95	120

only 68% degradation after 180 min. In addition, CMTS: Co consists exclusively of earth-abundant and non-toxic elements and demonstrates excellent structural and chemical stability over multiple photocatalytic cycles. A comparative overview of these studies is presented in Table 1.

Kinetic analysis serves as a fundamental tool for elucidating the mechanistic pathways involved in photocatalytic degradation processes. Fig. 13a shows a plot of $\ln(C_0/C)$ *vs.* irradiation time for CBTS: Co photocatalysts with different Co doping levels. C_0 is the initial concentration of RhB, while C is the concentration at the time of irradiation (t). The linearity of all curves indicates that the photodegradation of RhB follows a pseudo-first-order kinetics model, consistent with the Langmuir–Hinshelwood mechanism, which can be expressed by the following equation:[46]

$$\ln\left(\frac{C_0}{C_t}\right) = k_{app}t \quad (8)$$

C_0 represents the initial concentration of RhB, C_t is the concentration at irradiation time t, and K_{app} (min^{-1}) is the apparent rate constant.

The experimental data were fitted to the linearized form of the pseudo-first-order kinetic model, yielding a high correlation coefficient ($R^2 = 0.992$), which corroborates the suitability of this model in describing the photodegradation process. Furthermore, the linear correlation observed across all samples suggests a consistent degradation mechanism mainly driven by the availability and accessibility of active sites on the surface of the CBTS: Co photocatalysts. This uniform behavior implies that the photocatalytic process is surface-reaction limited, where the rate of RhB degradation is directly influenced by the number of catalytically active sites participating in the photogenerated charge transfer and subsequent radical-mediated reactions. The estimated apparent rate constants offer valuable insights into the underlying reaction mechanism, suggesting that the degradation of RhB occurs principally *via* a pseudo-first-order pathway, likely managed by the generation of reactive oxygen species (ROS) facilitated by the Co-doped CBTS photocatalyst under visible light irradiation. The values of K_{app} were extracted from the slopes of the respective linear fits, as shown in Fig. 13b. The K_{app} increases progressively with higher Co doping, confirming that Co incorporation enhances the photocatalytic activity of the CBTS films under visible light irradiation. Among all the samples, the CBTS: Co film with 6 at. Co-doping exhibited the highest K_{app}, approximately 3.5×10^{-3} min^{-1}, which is nearly three times greater than that of the undoped one. This significant enhancement reflects the most efficient degradation kinetics and confirms the superior

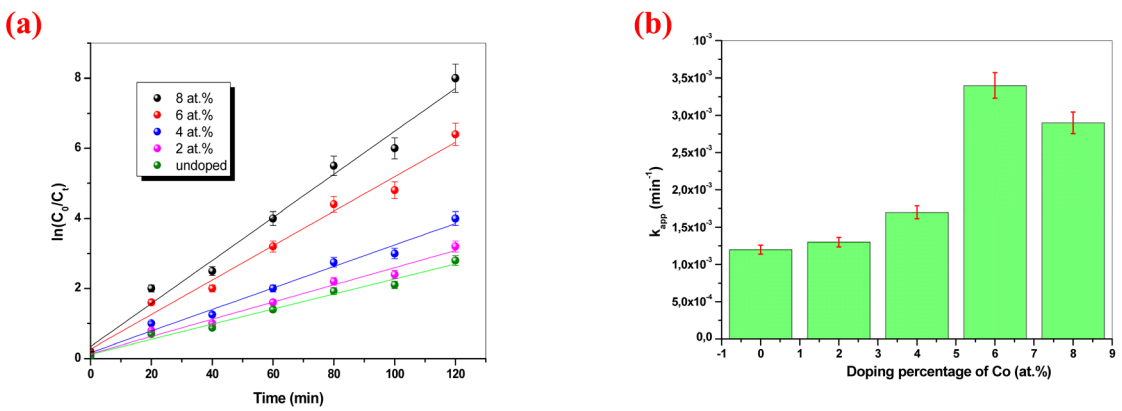

Fig. 13 (a) Pseudo-first-order kinetics: $\ln(C_0/C_t)$ *vs.* irradiation time for Co-doped CBTS photocatalysts, (b) variation of photodegradation rate constant with increasing Co content in CBTS films.

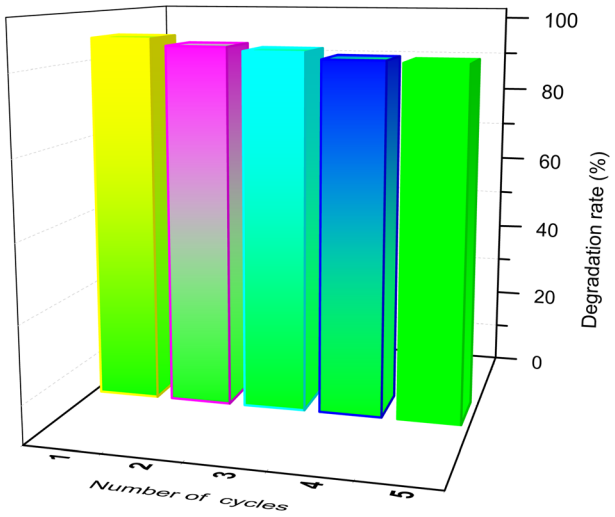

Fig. 14 Cycling test for the photocatalytic degradation of RhB in the presence of CBTS: Co (6 at%) catalysts.

photocatalytic performance of the optimally doped catalyst. This enhancement is likely attributed to enhanced charge carrier separation, increased surface-active sites, and improved visible-light absorption.

To assess the stability and recyclability of the CBTS: Co (6 at%) sample, a recycling test was carried out over five consecutive degradation cycles of RhB under visible light irradiation, as shown in Fig. 14. Between each cycle, the catalyst surface was carefully cleaned by rinsing with DI water to remove residual RhB dye and ensure reproducibility. Remarkably, only a slight decrease in photocatalytic rate was observed after five cycles, indicating that the CBTS: Co (6 at%) photocatalyst exhibits excellent stability. Nevertheless, the observed slight decrease in photocatalytic activity over five successive cycles might be attributed to surface contamination by reaction intermediates, partial catalyst loss during recovery, and potential degradation of active sites or structural integrity under increased light irradiation. To identify the types of ROS involved in the photocatalytic process of Co-doped CBTS (6 at%) thin films, EPR spectroscopy measurements were performed. As we all know, the photodegradation of organic pollutants is commonly attributed to photocatalytic processes facilitated by various ROS, including $^{\bullet}O_2^-$, $^{\bullet}OH$, e^-, and holes h^+, which synergistically contribute to the oxidative decomposition of organic contaminants.[52] Moreover, previous studies have demonstrated that the generation of ROS in chalcogenide-based materials starts upon visible light irradiation.[53] In this study, BMPO was used as a spin-trapping agent to detect the generation of $^{\bullet}O_2^-$ during the photocatalytic degradation processes. Under dark conditions, no signal was observed. Nevertheless, after 2 min of visible light irradiation, a characteristic quartet paramagnetic resonance signal with an intensity ratio of 1 : 2 : 2 : 1 appeared, confirming the formation of $^{\bullet}O_2^-$ during the photocatalytic reaction in the presence of CBTS: Co (6 at%) catalysts, as shown in Fig. 15a. After 6 min of light irradiation, the BMPO-$^{\bullet}O_2^-$ adduct signal increased, suggesting increased generation of $^{\bullet}O_2^-$ over time. Similarly, DMPO-$^{\bullet}OH$ adducts were detected, suggesting that $^{\bullet}OH$ radicals were generated during the photocatalytic process. The enhanced radical formation in the RhB dye can be attributed to improved charge transfer dynamics, facilitated by the CBTS: Co (6 at%) catalysts. This composition

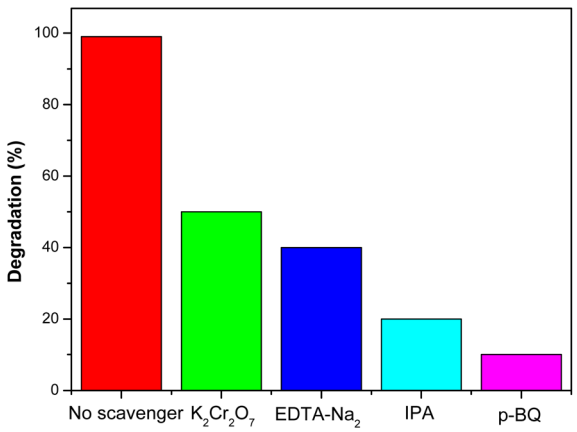

Fig. 16 Degradation rate of RhB dye in the presence of various scavengers under visible light.

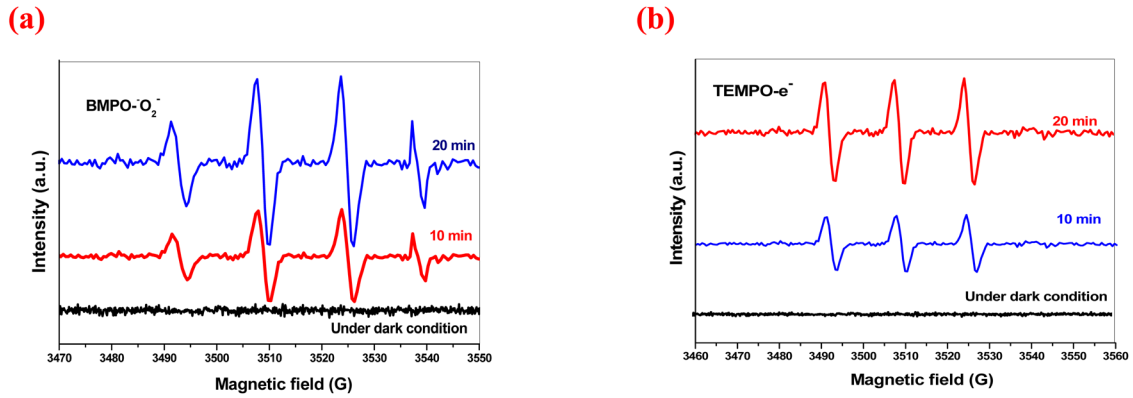

Fig. 15 EPR spectra of CBTS: Co (6 at%) catalysts for detecting (a) BMPO-$^{\bullet}O_2^-$ and (b) TEMPO-e^- under dark conditions and visible light irradiation.

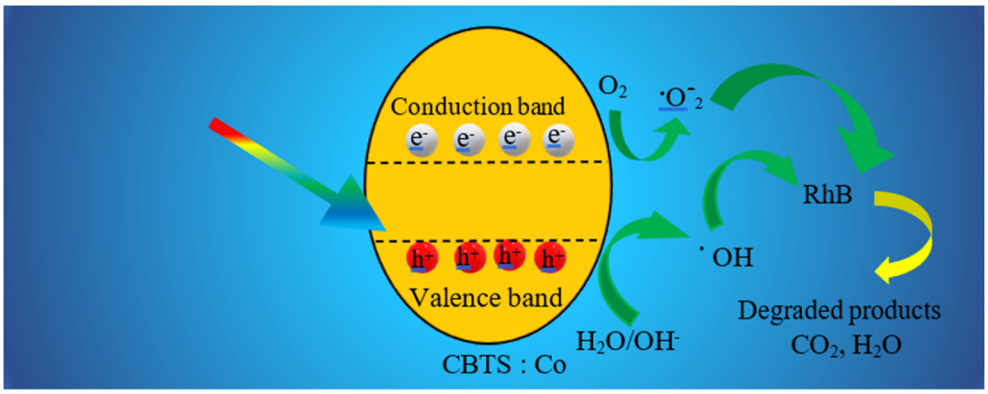

Fig. 17 Schematic illustration of the proposed reaction mechanism for RhB degradation over CBTS: Co (6 at%) catalysts under visible light irradiation.

promotes efficient separation of photogenerated e^-/h^+ pairs, thereby increasing the availability of charge carriers for radical generation. On the other hand, photoinduced e^- are also recognized as typical active species in photocatalytic processes, with TEMPO commonly employed as a trapping agent in EPR measurements to detect their presence. Under dark conditions, no signal was observed. Nevertheless, after 2 min of visible light irradiation, a stable triplet paramagnetic resonance peak with a 1 : 1 : 1 intensity ratio was observed, confirming the formation of e^- during the photocatalytic reaction, as shown in Fig. 15b. Upon 6 min of irradiation, the TEMPO-e^- adduct intensity was weakened, indicating the decline in the catalyst's ability to generate or transfer electrons under the given conditions over time. The signal intensity trend for photoinduced h^+ showed a similar pattern, attributed to the simultaneous formation of e^-/h^+ pairs. This outcome suggests that both $^{\bullet}OH$ and $^{\bullet}O_2^-$ radicals play crucial roles in the degradation of RhB dye, with the process mainly driven by the formation of $^{\bullet}O_2^-$ and $^{\bullet}OH$ radicals. To further corroborate this inference, quenching experiments were also performed to identify the specific radicals involved in the photocatalytic degradation of RhB in the studied system. Four different quenching trapping agents were used: $K_2Cr_2O_7$ (scavenger for e^-), EDTA-Na_2 (scavenger for h^+), IPA (scavenger for $^{\bullet}OH$), and *p*-BQ (scavenger for $^{\bullet}O_2^-$). These quenching agents were employed to evaluate the relative contribution of each ROS to the degradation of RhB dye. When IPA or *p*-BQ was added to the reaction system, the degradation performance of RhB on CBTS: Co (6 at) catalyst was considerably reduced to 10.2%, while the degradation was slightly decreased when $K_2Cr_2O_7$ was added. This indicates that $^{\bullet}O_2^-$ and $^{\bullet}OH$ play a major role in the degradation of RhB dye, while e^- and h^+ have little effect, as shown in Fig. 16. This outcome aligns well with the previously discussed EPR analysis. Moreover, the quenching experiments prove that all four species contribute to the photocatalytic degradation process of RhB dye, with their involvement following the order: $^{\bullet}O_2^- > {}^{\bullet}OH > e^- > h^+$.

Based on the previous results, the plausible mechanism for the degradation of RhB dye facilitated by CBTS: Co (6 at%) photocatalysts is illustrated in Fig. 17. Upon light irradiation, CBTS: Co (6 at%) absorbs photons with sufficient energy, resulting in the generation of (e^-/h^+) pairs. These charge carriers migrate to the surface of the CBTS: Co (6 at%) catalyst, where the photogenerated electrons reduce adsorbed oxygen (O_2) molecules to form $^{\bullet}O_2^-$, while the holes oxidize surface-bound water molecules to generate $^{\bullet}OH$. Both $^{\bullet}O_2^-$ and $^{\bullet}OH$ are reactive species that easily participate in the oxidative degradation of RhB organic dyes, ultimately leading to their mineralization. The overall photocatalytic degradation process facilitated by CBTS: Co (6 at%) photocatalysts can thus be described by the following sequential steps:

Photon absorption:

$$\text{CBTS: Co} + h\nu \rightarrow e^- + h^+ \quad (9)$$

Superoxide radical formation

$$e^- + O_2 \rightarrow {}^{\bullet}O_2^- \quad (10)$$

Hydroxyl radical generation:

$$h^+ + H_2O \rightarrow {}^{\bullet}OH \quad (11)$$

Dye degradation:

$$\text{RhB} + {}^{\bullet}O_2^-/{}^{\bullet}OH \rightarrow \text{degraded products} \rightarrow CO_2 + H_2O \quad (12)$$

4. Conclusion

This study demonstrates the successful incorporation of Co into CBTS thin films, resulting in notable enhancements in their photocatalytic activity for the degradation of RhB as an organic pollutant under visible light irradiation. Substitution of Co at the Ba^{2+} site was confirmed by XRD, Raman, and XPS analyses. The morphology of CBTS thin films reveals a reduction in particle size, which is advantageous for photocatalytic applications owing to the associated increase in surface area. The optical transmittance and band gap energy of CBTS thin films systematically vary with increasing Co doping level, showing reduced transmittance, enhanced reflectivity, and a broadened

band gap at higher doping levels, consistent with structural modifications and lattice strain induced by Co incorporation. Among all compositions, CBTS: Co (6 at%) exhibited the highest photocatalytic efficiency, achieving 95% RhB degradation within 120 min. These enhancements are attributed to synergistic effects of microstructural refinement, band structure tuning, and improved charge separation. Furthermore, quenching experiments and ESR analyses identified that all four species contribute to the photocatalytic degradation process of RhB dye, with their involvement following the order: $^{\bullet}O_2^- > {}^{\bullet}OH > e^- > h^+$. Overall, Co-doped CBTS presents itself as a promising, earth-abundant material for sustainable photocatalytic applications.

Author contributions

I am the sole author of this work, and no contributions from others were involved in its creation.

Conflicts of interest

The author confirms that there are no known competing financial interests or personal relationships associated with this publication for this work that could have influenced its outcome.

Data availability

The data supporting this article have been included as part of the supplementary information (SI). Supplementary information is available: the Raman modes of Cu_2BaSnS_4 supporting this study. See DOI: **https://doi.org/10.1039/d5ra05156h**.

Acknowledgements

I enthusiastically acknowledge financial support from the Center of Research and Technology of Energy, Technopole of Borj Cedria, Tunisia.

References

1 S. Hadke, M. Huang, C. Chen, Y. F. Tay, S. Chen, J. Tang and L. Wong, Emerging Chalcogenide Thin Films for Solar Energy Harvesting Devices, *Chem. Rev.*, 2022, **122**(11), 10170–10265.
2 M. M. Khan, Introduction and fundamentals of chalcogenides and chalcogenide-based nanomaterials, in *Chalcogenide-Based Nanomaterials as Photocatalysts*, Elsevier, 2021, pp. 1–6.
3 H. Zhao, Z. Jia, Y. Yang, Y. Liu and Q. Lin, Solution-processed $ZnBi_2S_4$ polycrystalline thin films for low noise photodetection, *Appl. Phys. Lett.*, 2024, **124**, 233302.
4 S. Mishra, P. Jaiswal, P. Lohia and D. K. Dwivedi, Chalcogenide glasses for sensor application: A Review, *IEEE Xplore*, 2018, 1–5.
5 H. Ishiguro, R. Nakano, Y. Yao, J. Kajioka, A. Fujishima, K. Sunada, M. Minoshima, K. Hashimoto and Y. Kubota, Photocatalytic inactivation of bacteriophages by TiO_2-coated glass plates under low-intensity, long-wavelength UV irradiation, *Photochem. Photobiol. Sci.*, 2011, **10**, 1825–1829.
6 D. Bhanderi, P. Lakhani and C. K. Modi, Graphitic carbon nitride (g-C_3N_4) as an emerging photocatalyst for sustainable environmental applications: a comprehensive review, *RSC Sustain.*, 2024, **2**, 265–287.
7 G. M. Fortes, A. L. da Silva, B. Ramos, J. Bettini, F. C. Fonseca, R. V. Gonçalves, O. R. Junior and D. Gouvea, Cl-Doped ZnO Nanoparticles with Enhanced Photocatalytic Activity via Selective Surface Lixiviation: Implications for Acetaminophen Degradation, *ACS Appl. Nano Mater.*, 2025, **8**(5), 2481–2492.
8 A. S. Kadari, A. N. Ech-Chergui, P. R. Ghediya, A. Guendouz, M. Guezzoul, O. El Khouja, A. E. Bocirnea, K. Driss-Khodja, B. Amrani and A. C. Galca, Growth and optimization of spray-coated Cu_2BaSnS_4 thin films for solar photovoltaic application, *Materialia*, 2024, **36**, 102178.
9 S. K. M, S. P. Madhusudanan, S. C. Kanth, *et al.*, Solution phase fabrication of photoactive Cu_2BaSnS_4 thin films for solar energy harvesting, *J. Solid State Electrochem.*, 2020, **24**, 305–311.
10 Jyoti and B. C. Mohanty, Barium concentration-controlled phase evolution in molecular solution processing of Cu_2BaSnS_4 thin films for solar cells with improved optical and electrical properties, *J. Alloys Compd.*, 2024, **986**, 174105.
11 M. S. Kumar, S. P. Madhusudanan and S. K. Batabyal, Solution-processed photoactive trigonal Cu_2BaSnS_4 thin films for efficient solar energy harvesting, *Mater. Charact.*, 2021, **174**, 110988.
12 A. Ali, S. Ahmed, J. Rehman, M. R. Abdullah, H.-B. Chen, B. Guo and Y. Yang, Cu_2BaSnS_4 novel quaternary quantum dots for enhanced photocatalytic applications, *Mater. Today Commun.*, 2011, **26**, 101675.
13 G. Hao, Z. Chen, R. Xian and W. Yifan, Synthesis and characterizations of Cu_2BaSnS_4 nanoparticles via solvothermal route, *Chalcogenide Lett.*, 2025, **22**, 255–260.
14 K. Kasinathan, J. Kennedy, M. Elayaperumal, *et al.*, Photodegradation of organic pollutants RhB dye using UV simulated sunlight on ceria-based TiO_2 nanomaterials for antibacterial applications, *Sci. Rep.*, 2016, **6**, 38064.
15 X. Zhang, P. Tang, G. Zhai, X. Lin, Q. Zhang, J. Chen and X. Wei, Regulating Phase Junction and Oxygen Vacancies of TiO_2 Nanoarrays for Boosted Photoelectrochemical Water Oxidation, *Chem. Res. Chin. Univ.*, 2022, **38**(5), 1292–1300.
16 N. P. F. Gonçalves, M. C. Paganini, P. Armillotta, E. Cerrato and P. Calza, The Effect of Cobalt Doping on the Efficiency of Semiconductor Oxides in the photocatalytic Water Remediation, *J. Environ. Chem. Eng.*, 2019, **7**(6), 103475.
17 T. H. Qamar, S. ul Hassan, N. Ahmed, S. B. Jamali, K. Kausar, S. Huang and L. Deng, Cobalt/nitrogen doped noodle-like carbon nanotubes composites with heterogeneous interfaces for efficient electromagnetic wave absorption, *Phys. Scr.*, 2025, **100**, 055937.

18 S. Zemene, Y. B. Yohannes and G. A. Wubetu, Synthesis and characterization of undoped and Co-doped Bismuth Ferrite nanoparticles for photovoltaic applications, *Phys. Scri.*, 2025, **100**, 0159a5.
19 E. El Mahboub, O. El Khouja, A. E. Bocirnea, S. Zakaria, A. C. Galca, M. Mansori and A. E. Hichou, Investigation of kesterite to stannite phase transition and band gap engineering in $Cu_2Zn_{1-x}Co_xSnS_4$ thin films prepared by sol-gel spin coating, *Appl. Surf. Sci.*, 2024, **672**, 160848.
20 T. Degen, M. Sadki, E. Bron, U. König and G. Nénert, The HighScore suite, *Powder Diffr.*, 2014, **29**, S13–S18.
21 D. Nečas and P. Klapetek, *Cent. Eur. J. Phys.*, 2012, **10**(1), 181.
22 Z. Chen, K. Sun, Z. Su, F. Liu, D. Tang, H. Xiao, L. Shi, L. Jiang, X. Hao and Y. Lai, Solution-Processed Trigonal Cu_2BaSnS_4 Thin-Film Solar Cells, *ACS Appl. Energy Mater.*, 2018, **1**(7), 3420–3427.
23 X. Geng, T. Chang, J. Fan, Y. Wang, X. Wang, Y. Sun, P. Selvarajan, C. Liu, C.-H. Lin, X. Wang, J. Yang, Z. Cheng, K. Kalantar-Zadeh, X. Cao, D. Wang, A. Vin, J. Yi and T. Wu, *ACS Appl. Mater. Interfaces*, 2022, **14**(17), 19736–19746.
24 A. M. Abdulwahab, A. A. AL-Adhreai, A. H. Al-Hammadi, A. Al-Adhreai, A. Salem, F. K. Alanazi and M. ALSaeedy, Synthesis, characterization, and anti-cancer activity evaluation of Ba-doped CuS nanostructures synthesized by the co-precipitation method, *RSC Adv.*, 2025, **15**, 4669–4680.
25 T. Abza, D. G. Dadi, F. G. Hone, T. C. Meharu, G. Tekle, E. B. Abebe and K. S. Ahmed, Characterization of Cobalt Sulfide Thin Films Synthesized from Acidic Chemical Baths, *Adv. Mater. Sci. Eng.*, 2020, **2020**, 2628706.
26 A. Chihi, Impact of Ag-coating on CAS thin film for boosted photoelectrochemical water splitting, *Appl. Phys. A*, 2023, **129**, 472.
27 A. Chihi, Gamma-irradiated stibnite thin films set a remarkable benchmark performance for photoelectrochemical water splitting, *RSC Adv.*, 2024, **14**, 12475–12495.
28 H. Luo, J. Chen, X. Zhang, S. Wang, H. Gu, W. Wang and H. Li, Controlled synthesis of high efficiency Cu_2BaSnS_4 solar cells via a solution-processed method, *Mater. Lett.*, 2020, **270**, 127750.
29 D. Essossimna and S. Jinzhan, First spray pyrolysis thin film fabrication of environment-friendly Cu_2BaSnS_4 (CBTS) nanomaterials, *Chem. Phys. Lett.*, 2021, **770**, 138406.
30 A. Ait-Karra, O. Zakir, A. Mourak, M. Lasri, R. Idouhli, A. Abouelfida, M. E. Khadiri and J. Benzakour, A Comprehensive Structural, Morphological, and Electrochemical Analysis of Electrodeposited Cobalt Sulfide Thin Films, *J. Electrochem. Soc.*, 2025, **172**, 052503.
31 U. B. R, G. Rajamanickam, M. Deshpande and J. B. Revealing, high-performance supercapacitor: Synergistic cobalt sulfide/reduced graphene oxide nanocomposite for enhanced energy storage, *Int. J. Hydrogen Energy*, 2025, **129**, 38–50.
32 S. G. Lyapin, A. N. Utyuzh, A. E. Petrova, A. P. Novikov, T. A. Lograsso and S. M. Stishov, Raman studies of nearly half-metallic ferromagnetic CoS_2, *J. Phys.: Condens. Matter*, 2014, **26**, 396001.
33 A. Chihi, Effect of Ruthenium doping in tailoring structure, optical and electrical properties of Sb_2S_3 thin films synthesised via electrodeposition technique, *J. Mater. Sci.: Mater. Electron.*, 2023, **34**, 2087.
34 S. Saedy, N. Hiemstra, D. Benz, H. V. Bui, M. Nolan and J. R. v. Ommen, Dual promotional effect of Cu_xO clusters grown with atomic layer deposition on TiO_2 for photocatalytic hydrogen production, *Catal. Sci. Technol.*, 2022, **12**, 4511–4523.
35 S. Dudziak, Z. Ryżyńska, Z. Bielan, J. Ryl, T. Klimczuk and A. Zielińska-Jurek, Pseudo-superparamagnetic behaviour of barium hexaferrite particles, *RSC Adv.*, 2020, **10**, 18784–18796.
36 R. Félix, N. Llobera-Vila, C. Hartmann, C. Klimm, M. Hartig, R. G. Wilksac and M. Bär, Preparation and in-system study of $SnCl_2$ precursor layers: towards vacuum-based synthesis of Pb-free perovskites, *RSC Adv.*, 2018, **8**, 67–73.
37 Y. Fang, X. Chen, C. Yin and L. Cui, Boosting the capacitive property of cobalt sulfide through interface engineering for high-performance supercapacitors, *Ceram. Int.*, 2021, **47**, 24973–24981.
38 Y. Lykhach, S. Piccinin, T. Skála, N. Tsud, O. Brummel, M. F. Camellone, K. Beranová, A. Neitzel, S. Fabris, K. C. Prince, V. Matolín and J. Libuda, Quantitative Analysis of the Oxidation State of Cobalt Oxides by Resonant Photoemission Spectroscopy, *J. Phys. Chem. Lett.*, 2019, **10**(20), 6129–6136.
39 J. Zhu, Z. Ren, S. Du, Y. Xie, J. Wu, H. Meng, Y. Xue and H. Fu, Co-vacancy-rich $Co_{1-x}S$ nanosheets anchored on rGO for high-efficiency oxygen evolution, *Nano Res.*, 2017, **10**, 1819–1831.
40 A. Chihi and B. Bessais, Characterization and photoelectrochemical properties of CICS thin films grown *via* an electrodeposition route, *RSC Adv.*, 2017, **7**, 29469–29480.
41 A. Chihi, Tailoring the photoelectrochemical water splitting of $CuSbS_2$ thin films by artificial defect engineering based on Bi doping, *Eur. Phys. J. Plus*, 2023, **138**, 803.
42 M. Sultana, *et al.*, Strategic development of metal-doped TiO_2 photocatalysts for enhanced dye degradation activity under UV-Vis irradiation: A review, *Curr. Res. Green Sustainable Chem.*, 2023, **7**, 100383.
43 P. Dixit, V. Chauhan, S. B. Rai and P. C. Pandey, Realization of neutral white light emission in $CaMoO_4$:$4Dy^{3+}$ phosphor via Sm^{3+} co-doping, *J. Alloys Compd.*, 2022, **897**, 162820.
44 O. V. Rambadey, A. Kumar, A. Sati and P. R. Sagdeo, Exploring the Interrelation between Urbach Energy and Dielectric Constant in Hf-Substituted $BaTiO_3$, *ACS Omega*, 2021, **6**(47), 32231–32238.
45 M. A. Sayeed and H. K. Rouf, Effect of Zn-doping on the structural, optical and electrical properties of thermally vacuum evaporated CdTe thin films, *Surf. Interfaces*, 2021, **23**, 100968.
46 S. Goktas and A. Goktas, A comparative study on recent progress in efficient ZnO-based nanocomposite and

heterojunction photocatalysts: A review, *J. Alloys Compd.*, 2021, **863**, 1–25.

47 M. Pannerselvam, A. Shameem, N. Dineshbabu, A. Murugan, T. Bavani and V. Siva, A nanoscale tungsten disulfide decorated polypyrrole nanocomposites for effective photocatalytic degradation of Rhodamine B under visible light, *J. Mol. Struct.*, 2025, **1347**, 143272.

48 G. Chen, M. Yang, B. Tian, J. Yao, S. Chen, D. Li and G. Yuan, Cu-doped ZnO nanoparticles and its application for the photocatalytic degradation of Rhodamine B, *Sci. Rep.*, 2025, **15**, 18246.

49 Y. Wang, Y. Pan, S. He and R. Huang, Eu/Fe Co-doped Bi_2WO_6 nanocatalyst: Synergistic photo-Fenton catalysis for rapid dye degradation with robust pH tolerance and ecological safety, *Mater. Chem. Phys.*, 2025, **346**, 131401.

50 Y. Zhao, H. Shi, D. Yang, J. Fan, X. Hu and E. Liu, Fabrication of a Sb_2MoO_6/g-C_3N_4 Photocatalyst for Enhanced RhB Degradation and H_2 Generation, *J. Phys. Chem. C*, 2020, **124**(25), 13771–13778.

51 M. Saha, P. P. Cho, C. Subrahmanyam, M. K. Niranjan and S. Asthana, Structural, dielectric, optical and photocatalytic properties of $(Na_{0.5}Bi_{0.5})$ ZrO_3 lead-free perovskite: insights from experimental and ab initio theoretical studies, *J. Phys. D: Appl. Phys.*, 2025, **58**, 085304.

52 J. Tang, J. Li, Y. Cheng, P. Huang and Q. Deng, Facile hydrothermal-carbonization preparation of carbon-modified Sb_2S_3 composites for photocatalytic degradation of methyl orange dyes, *Vacuum*, 2015, **120**, 96–100.

53 I. Radja, A. N. Ech-Chergui, A. Zekri, A. Rahman, Y. Khane, F. Bennabi, A. S. Kadari, M. Guezzoul, A. Popa, K. Driss-Khodja, B. Aïssa, B. Amrani and M. M. Khan, Influence of Cu doping on the functionality of spray-coated SnS_2 thin films and its photocatalytic degradation of dyes and antibacterial activity, *Phys. Scr.*, 2024, **99**, 065966.